The Effect of Hydrogen on Non-linear Flame Saturation

Eirik Æsøy
Department of Energy
and Process Engineering,
Norwegian University of Science
and Technology,
Trondheim N-7491, Norway
Email: eirik.asoy@ntnu.no

Thomas Indlekofer
SINTEF Energy Research,
Trondheim N-7465, Norway

Mirko R. Bothien
Institute of Energy Systems
and Fluid Engineering,
Zurich University
of Applied Sciences ZHAW,
Zurich, Switzerland

James R. Dawson
Department of Energy
and Process Engineering,
Norwegian University of Science
and Technology,
Trondheim N-7491, Norway

We investigate the effect of increasing levels of hydrogen enrichment on the non-linear response and saturation of premixed bluff-body stabilised methane/hydrogen flames submitted to acoustic forcing. The thermal power is kept approximately constant to preserve the nozzle velocity whilst increasing the flame speed through hydrogen enrichment. The flame describing function (FDF) is measured for a fixed frequency and three hydrogen-methane blends ranging from 10% *to* 50% *by power, corresponding to* 25% *to* 75% *by volume. We show that when the flame is forced at the same frequency at similar power and bulk velocities, increasing levels of hydrogen enrichment increase the saturation amplitude of the flame. To provide insight into the flame dynamics responsible for the change in the global non-linear response and saturation amplitude, the flames were investigated using high-speed imaging in combination with OH-PLIF at a range of forcing amplitudes. At lower hydrogen concentrations, the flame is stabilised along the inner shear layer and saturation in the heat release rate occurs at lower forcing amplitudes due to large-scale flame-vortex interactions causing flame annihilation as observed in several previous studies. At increased levels of hydrogen enrichment, distinctly different flame dynamics are observed. In these cases, the flame accelerates and propagates across to the outer shear layer which acts to suppress large-scale flame annihilation during roll-up of both the inner and outer shear layers. This results in a coherent increase in flame surface area with forcing amplitudes significantly increasing the saturation amplitude of the flame. These results show that high levels of hydrogen increase the amplitude response to acoustic forcing leading to higher saturation amplitudes. This suggests that substituting natural gas with hydrogen in Gas Turbines increases the risk of much higher limit-cycle amplitudes if self-excited instabilities occur.*

1 Introduction

Developing the technology to burn hydrogen in stationary gas turbines may provide a crucial building block towards zero-carbon power generation. During periods of excess energy production renewable energy sources can be used to produce hydrogen which can be easily stored and utilised to provide energy on demand. However, hydrogen has significantly different combustion properties from hydrocarbon fuels as it is extremely diffusive, has significantly higher flame speeds, extinction strain rates and an unknown pressure dependence [1; 2; 3; 4; 5; 6]. Since current gas turbine technology is optimised around hydrocarbon fuels, shifting to hydrogen poses new technical and scientific challenges in terms of thermoacoustic instabilities [7; 8; 9; 10; 11] and flashback [12; 13]. Understanding the fundamental effects of hydrogen will aid in the development of new combustor technologies needed to enable and ensure stable operation [14; 15; 16; 17; 18].

Recently there has been a large effort studying the effect of hydrogen on combustion dynamics. Increasing levels of hydrogen concentration have been shown to have a large effect on the mean flame stabilisation where the flame tends to become shorter, more compact and stabilises close to the flame holder [19; 20; 21; 22; 23; 24; 7]. Shorter flames respond to acoustic velocity fluctuations over a higher range of frequencies. This can be quantified through a Flame Transfer Function (FTF) which relates the fluctuations in the heat release rate of the flame to an imposed acoustic velocity fluctuation [25]. Overall, it has been shown that increasingly compact premixed flames result in an increase in the gain cut-off frequency and a reduced time-delay [26; 27; 28; 29; 30]. The increased cut-off frequency of hydrogen enriched premixed flames can also make them more susceptible to convective disturbances which could be used for control [27; 31; 32]. Undesirable effects due to the increase in the cut-off frequency have also been observed in mesoscale burners where thermoacoustic modes were triggered at higher frequencies compared to natural gas [9; 10; 11; 33; 34]. This change in behaviour has been observed in annular and can type burners [35; 36; 37]. Other studies have shown that strategic secondary hydrogen injection in small mass fractions can increase flame stability [38; 39; 40]. Overall, these studies demonstrate that the effects of hydrogen can have both detrimental or beneficial effects.

Most of these studies to date have focused on the system behaviour or on the linear flame response. As the FTF is only valid in the limit of small perturbations and therefore restricted to the linear response, capturing the instability amplitude requires a characterisation of the non-linear behaviour of the flame response [41; 42] which is often related to the coupling between the flame and flow dynamics [43; 44]. The flame response saturates when submitted to sufficiently high acoustic amplitude oscillations and is generally attributed to vortex-flame interactions [45; 46; 47] which limit fluctuations in the heat release rate through the destruction of the flame surface via flame annihilation.

The aim of this paper is to investigate the effect of high levels of hydrogen concentration on the non-linear response of hydrogen-methane flames and the underlying changes in the flame dynamics for similar thermal power and bulk velocities. We measure the flame response over a range of hydrogen/methane blends and we investigate how the flame and flow interact and how this interaction affects their non-linear relationship.

The paper is structured as follows: First, the experimental setup and the methodology are described. Then, global flame response measurements in form of FDFs are presented for various levels of hydrogen enrichment. Finally, details on the flame dynamics and its relation to vortex-roll up are presented and discussed.

2 Experimental setup

2.1 Burner setup

The experimental setup is shown schematically in Fig. 1 and follows a similar setup to previous studies [26; 8]. The burner was designed to produce premixed flames that stabilise in the wake of a bluff body with a diameter $d_b = 13\,\text{mm}$ which has an inclination angle of 45°. The bluff body was centred in a $L_p = 160\,\text{mm}$ long and $d_p = 19\,\text{mm}$ diameter pipe by a $d_r = 5\,\text{mm}$ rod. After the contraction of the bluff body, the flow expands freely into the open environment (unconfined).

Alicat mass flow controllers (MFCs) were used to regulate the air and fuel (H_2 and CH_4) mass flows with a variation of less than 1%. The gases were mixed sufficiently far upstream to achieve premixed conditions. The flow was contracted through the bottom of a plenum section before being converged into the injector pipe as indicated by the streamlines in Fig. 1.

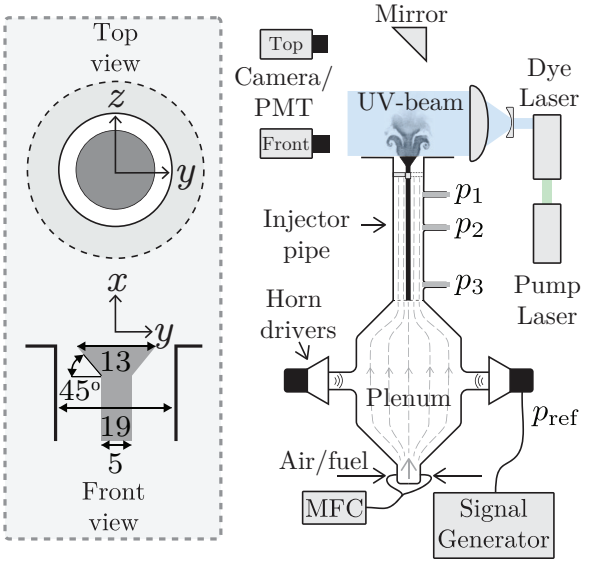

Fig. 1. Burner setup and measurement diagnostics. Dimensions are given in mm. For more details see [48].

2.2 Measurement diagnostics

Acoustic pressure oscillations p_{1-3} were measured at three axial locations $x = -45, -70$, and -130 mm, in the injector pipe by Kulite XCS-093-0.35D (range $0-35$ kPa) pressure transducers. The pressure signals were amplified by a Fylde FE-579-TA bridge amplifier and sampled at a rate of 51.2 kHz with a 24-bit NI-9234 DAQ. To externally excite/force the flow, two Monacor KU-516 horn drivers were mounted in the plenum. The forcing signals p_{ref} were monochromatic and generated using an Aim-TTi TGA1244 signal generator. The signal p_{ref} was also sampled to be used as a reference for cross power spectral analysis.

The acoustic field in the injector pipe was reconstructed by combining recordings of the pressure time-series and using the multiple microphone method (MMM) [49; 48]. The 1D acoustic pressure and velocity fields in the injector pipe are described by

$$\hat{p}_a(x) = A^+ \exp(-\mathrm{j}k_+ x) + A^- \exp(\mathrm{j}k_- x) \tag{1a}$$

$$\hat{u}_a(x) = \frac{1}{\rho c}\left(A^+ \exp(-\mathrm{j}k_+ x) - A^- \exp(\mathrm{j}k_- x)\right), \tag{1b}$$

where A^+ and A^- represent upstream and downstream propagating 1D acoustic waves, ρ and c are the gas density and the speed of sound respectively, and $k_\pm = k/(1 \pm \bar{u}/c)$ is the wave number $k = 2\pi f/c$. By including the area jump due to the bluff body, the acoustic velocity at the dump plane is given by

$$\hat{u} = \frac{A_p}{A_b}\hat{u}_a(x=0), \tag{2}$$

where the area ratio is given by $A_p/A_b = 1.75$. The area jump is assumed compact and the effect on the acoustic pressure is assumed to be small. The amplitude of the acoustic forcing $A = |\hat{u}|/\bar{u}$ was achieved by tuning the amplitude of p_{ref} through an iterative scheme as described in [48]. Fig. 2 shows the reconstructed acoustic mode inside the injector pipe where A is tuned in the range of $0.05-0.5$ in steps of 0.05 for $f = 1$ kHz. This frequency corresponds to the half-mode of the injector pipe and hence, large velocity fluctuations could be achieved at the dump plane.

All complex amplitudes, denoted by hatted quantities $(\hat{\cdot})$, are calculated by

$$\hat{p}_i = \frac{\mathrm{PSD}(p_{\text{ref}}, p_i')}{\sqrt{\mathrm{PSD}(p_{\text{ref}}, p_{\text{ref}})}}, \tag{3}$$

where PSD denotes the energy spectra estimated using the Welch method. The signals were binned into 50% overlapping windows and pre-multiplied by a Hanning window prior to the computation of the PSD.

An estimate of the fluctuations in the global heat release rate (HRR) was obtained through OH* and CH* light-

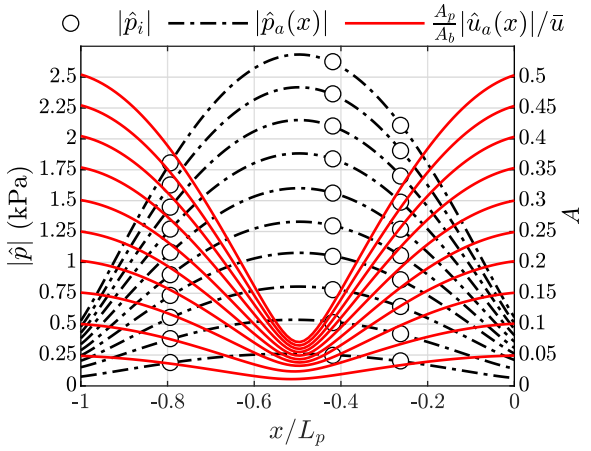

Fig. 2. Reconstructed acoustic mode inside the injector pipe forced at $f = 1$ kHz for increasing forcing amplitudes A. Markers $|\hat{p}_i|$ indicate measured pressure amplitudes and lines are obtained from Eq. (1).

emmisions using two Hamamatsu H11902-113 photomultiplier tubes (PMT) equipped with UV band pass filters, 310 ± 10nm for OH* and 430 ± 10nm for CH*. Since the air-fuel mixture was considered perfectly premixed, the chemiluminescence intensity is proportional to the global HRR ($I/\bar{I} = Q/\bar{Q}$) [50; 51; 48].

The flame response to acoustic forcing is quantified through the flame describing function (FDF) given by

$$\mathrm{FDF}(\omega, A) = \frac{\hat{Q}/\bar{Q}}{\hat{u}/\bar{u}} = G\exp(j\theta), \tag{4}$$

where G is the gain and θ the phase. The FDF relates the normalised fluctuations in HRR to the normalised fluctuations of the acoustic velocity $\hat{u}/\bar{u}$ at a frequency $2\pi f = \omega$ and normalised forcing amplitude $A = |\hat{u}|/\bar{u}$. In the low amplitude regime, there is a linear relationship between $\hat{Q}$ and $\hat{u}$, i.e. G and θ are not functions of A but only ω. In this regime, the global flame dynamics are described by the flame transfer function (FTF) and in [26; 8] we focused on the effect of hydrogen enrichment on the linear flame response. In this paper we consider large amplitude oscillations where the dependency of $\hat{Q}$ with $\hat{u}$ becomes non-linear and saturates.

The spatial distribution of HRR was obtained through images of OH* taken in the $x-y$ and $y-z$ planes using two Phantom V2012 high speed cameras, each equipped with a LaVision Intensified Relay Optics (IRO) unit, a Cerco 2178 UV lens (100F/2.8), and a UV filter (310(10) nm). These images represent a line of sight integrated view and are denoted q_z and q_x for the projections taken in the $x-y$ and $y-z$ planes respectively. The image and PMT intensity signals are normalised such that spatial integration provides the thermal power, i.e. $\mathrm{P} = \bar{I} = \int_V q\,\mathrm{dV}$. In this way the PMT and camera provide very similar signals as shown in [8].

To investigate the flame roll-up process that influences the non-linear flame dynamics, the planar flame front posi-

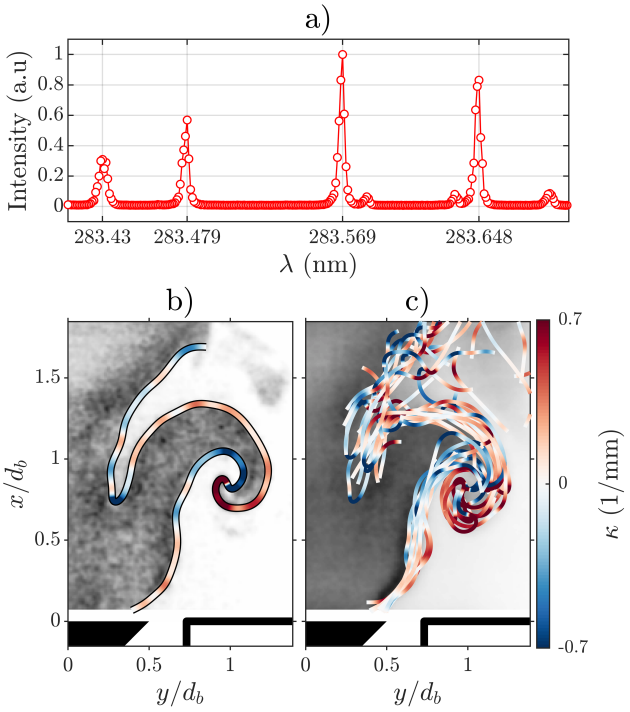

Fig. 3. a) OH-emission spectrum at different excitation wavelengths. b) A single snap-shot of an OH-PLIF signal and the computed flame surface $(x_s(l), y_s(l))$ coloured by flame curvature κ. c) Ensemble of phase-locked snap-shots superimposed.

tions and the flame curvature were obtained using high-speed OH-PLIF in the $x-y$ plane [52]. The system was comprised of an Edgewave IS400-2-L nd:YAG (532 nm) laser pumping a Sirah Credo-Dye-N laser providing an output pulse energy of about 0.3 mJ at a rate of 10 kHz. The beam was directed through a set of spherical and cylindrical lenses and collimated into a ≈ 1 mm thick and ≈ 50 mm high laser sheet, cutting the flame through the center of the bluff body. The output wavelength λ was tuned to match the intensity peak of the OH-radicals at 283.569 nm as shown in Fig. 3 a). The front camera was used with the intensifier gate time reduced to 80 ns to capture only the signal excited by the laser.

The flame front position is located close to the edges in the images where the intensity gradient is high. To extract the coordinates of the flame surface and compute the flame curvature, we follow the same processing steps as was described in [31]. These provide a set of flame surface coordinates $(x_s(l), y_s(l))$ which are parameterised by the arc length l. The flame curvature κ is calculated by

$$\kappa = \frac{\dot{x}_s \ddot{y}_s - \dot{y}_s \ddot{x}_s}{[\dot{x}_s^2 + \dot{y}_s^2]^{3/2}}, \tag{5}$$

where the dot denotes a derivative with respect to the arc length, $\dot{x}_s = \partial x_s / \partial l$. The curvature κ is positive when the flame is concave towards the unburnt reactants and negative when it is convex towards the unburnt reactants. An example of an OH-PLIF image and the instantaneous flame front coloured by curvature is shown in Fig. 3 b). For selected cases, an ensemble of 10000 phase-locked images was taken, resulting in 1000 images at 10 different phases relative to the forcing signal. Averaging data in each phase results in a phase averaged flame surface density (FSD) and a corresponding distribution of flame curvature. In Fig. 3 c), 15 ensembles are superimposed to illustrate this process.

3 Operating conditions and flame properties

The operating conditions are summarised in Table 1. For all cases, the thermal power and equivalence ratio were kept constant at $P = 7$ kW and $\Phi = 0.7$. The hydrogen concentration in terms of a power fraction was increased from $P_H = 0.1$ to $P_H = 0.5$. This was chosen intentionally to preserve the exit velocities at $\bar{u} \approx 20$m/s, and correspond to a Reynolds number of $Re = 1.4 \times 10^4$ based on the bluff body diameter. No self-excited instabilities were encountered for these conditions which allowed us to investigate the flame dynamics through external acoustic forcing. For $P_H > 0.5$ the flame flashed back into the injector pipe. Keeping the power and inlet velocities similar enables us to isolate the effect of hydrogen (fuel composition) on the non-linear interaction between the flow and the flame roll-up process when excited at the same frequency. Since the flow velocity and forcing frequency were kept constant, a Strouhal number based on the bluff body diameter $St_{d_b} = f d_b / \bar{u} = 0.65$ was preserved.

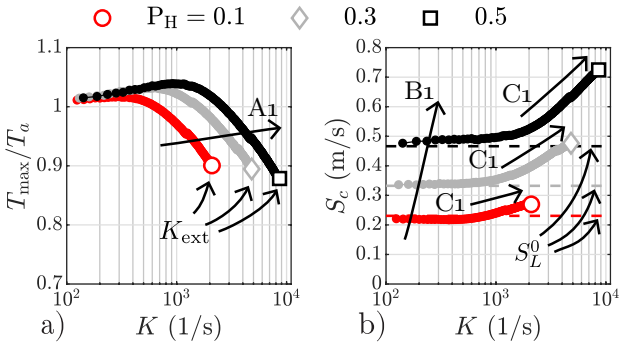

Fig. 4. Flame properties obtained using Cantera [53]. a) Upper branch of the "S-curve" plotting T_{max} against strain K. The extinction strain rates κ_{ext} are indicated by open symbols. b) Effect of strain rate on the consumption speed S_c, where S_L^0 is the unstretched laminar flame speed.

Changing the fuel also leads to changes in flame properties. A common way to obtain properties, such as the laminar flame speed, extinction strain rate, adiabatic flame temperature, etc., is to solve a 1D laminar flame problem numerically. For this purpose, solutions were obtained using Cantera with the GRI-Mech 3.0 reaction mechanism, multi-component mass diffusion and including the Soret effect [53], following a similar method as in [54; 55]. It should

Case	P (kW)	$\bar{u}$ (m/s)	$\mathrm{Re}_{d_b} = \bar{u}d_b/\nu$	$\mathrm{P_H}$	$\mathrm{V_H}$	Φ	T_a (°C)	S_L^0 (m/s)	K_{ext} (1/s)	f (kHz)	$\mathrm{St}_{d_b} = fd_b/\bar{u}$	$f\tau = fL_f/\bar{u}$
1	7	20.5	1.4×10^4	0.1	0.25	0.7	1848	0.23	2100	1	0.65	1.23
2	7	20.1	1.4×10^4	0.3	0.57	0.7	1876	0.33	4814	1	0.65	1.08
3	7	19.8	1.4×10^4	0.5	0.75	0.7	1904	0.47	8630	1	0.65	0.85

Table 1. Summary of operating conditions. P is the thermal power, $\bar{u}$ the bulk velocity at the dump plane, Re_{d_b} the Reynolds number based on the bluff body diameter. $\mathrm{P_H}$ and $\mathrm{V_H}$ are respectively the power and volume fractions of hydrogen in the fuel mixture, and Φ is the equivalence ratio. The parameters T_a, S_L^0, and K_{ext} are the adiabatic flame temperature, unstretched laminar flame speed, and the extinction strain rate respectively. The external forcing frequency is f, and St_{d_b} and $f\tau$ are normalised forcing frequencies.

be emphasised that these quantities do not include all the effects encountered in a turbulent flame and hence, they are only used here to substantiate the discussion of trends observed in the experiments.

To obtain the extinction strain rate and consumption speed for the different fuels when submitted to different levels of hydrodynamic strain $K = |\mathrm{d}u/\mathrm{d}x|_{\max}$, a premixed counter flow flame was solved with different inlet velocities. Fig. 4 a) shows the top branch of the S-curve plotting the maximum temperature against strain rate. The temperature is normalised by the adiabatic flame temperature T_a. The extinction strain rate K_{ext} is obtained when the flame is located at the boundary of the domain and no stable burning solution can be obtained. As indicated by the arrow annotated by $\mathrm{A_1}$, K_{ext} increases significantly with $\mathrm{P_H}$. This effect was also shown by [56], where hydrogen-enriched ammonia featured a significantly higher blow-off limit compared to methane.

Another important quantity is the propagation speed of the flame. A consumption speed S_c was computed by

$$S_c = \frac{1}{\rho_u c_p (T_b - T_u)} \int_{-\infty}^{\infty} q \mathrm{d}x, \tag{6}$$

where ρ_u, c_p, T_b, T_u, q are the reactant density, mass-specific heat, burnt and unburnt temperatures, and heat release rate respectively [57]. The consumption speed is shown in Fig. 4 b) and the unstretched laminar flame speed S_L^0, which is indicated by the dotted lines, was obtained by solving a freely-propagating flame. An increase in $\mathrm{P_H}$ leads to an increase in the flame speed annotated $\mathrm{B_1}$. Moreover, due to differential diffusion, there is an increase in the flame speed with the strain rate [1; 55]. This effect is annotated by $\mathrm{C_1}$ and is stronger for higher concentrations of hydrogen. Changes to these properties become important when discussing the kinematics of the flame vortex roll-up.

4 Mean flames

First, we investigate the effect of $\mathrm{P_H}$ on the mean flame shapes and discuss the implications these have for the flame dynamics. The mean OH* flame images viewed from the front are shown in Fig. 5 and the flame length L_f (red dotted lines) is calculated as the centre of heat release rate

$$L_f = \int_0^{\infty} x q_y \mathrm{d}x \Big/ \int_0^{\infty} q_y \mathrm{d}x, \tag{7}$$

from the stream wise profiles q_y, which are shown for the different flames in Fig. 5b).

Increasing $\mathrm{P_H}$ for a fixed Φ results in an increase in the laminar flame speed S_L^0 and a shorter flame length L_f as was discussed in [7]. This leads to a reduced convective time-delay $\tau = L_f/\bar{u}$, which represents the time it takes for a convective structure to move from the dump plane to L_f with an average velocity $\bar{u}$. The variation of τ with $\mathrm{P_H}$ is shown in Fig. 5 c) and shows a monotonic decrease as the hydrogen concentration is increased.

The forcing frequency that was chosen to investigate large amplitude forcing was $f = 1\,\mathrm{kHz}$. This frequency corresponds to a resonant acoustic mode of the injector pipe and hence, large amplitude forcing could be achieved (see Fig. 2). However, it is important to note that this corresponds to different frequencies when normalised by the convection time τ. As was shown in [8], τ changes inversely with the gain cut-off frequency of the FTF. This implies that hydrogen enrichment causes a flame to be more compact and hence, responds over a wider range of frequencies. In Table 1, $f\tau = fL_f/\bar{u}$ is shown for all cases. The flame is forced at different values of $f\tau$ and hence, a different gain and phase response can be expected. However, in this study, the aim is to preserve the hydrodynamics structure, and by varying the fuel and not the flow, the Strouhal number $\mathrm{St}_{d_b} = fd_b/\bar{u} = 0.65$ is preserved.

5 The Non-linear Flame Response

Focus is now directed towards the flame response to high amplitude forcing. In Fig. 6 a) the amplitude of $\hat{Q}$ is plotted as a function of A for all operating conditions. The gain is given by the average slope, i.e. when $\hat{Q}$ is normalised by A. We define the saturation amplitude as the point when $\hat{Q}$ reaches a constant value in the limit $\lim_{A\to\infty}$, which corresponds to $G = 0$. The phase relationship between $\hat{Q}$ and $\hat{u}$ is shown in Fig. 6 b).

The three cases show a typical behavior, where $\hat{Q}$ first increases linearly with A, before the relationship starts to level off and flatten [58; 46]. There is a clear trend in how

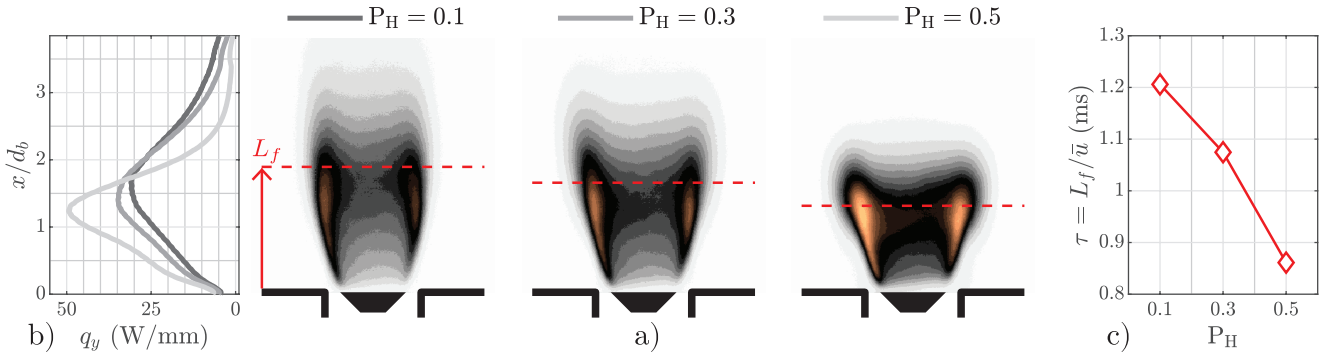

Fig. 5. a) Mean flame images. The red dashed lines indicate the center of heat release rate L_f computed from the stream-wise profiles q_y shown in b). c) The time-delay τ plotted vs P_H.

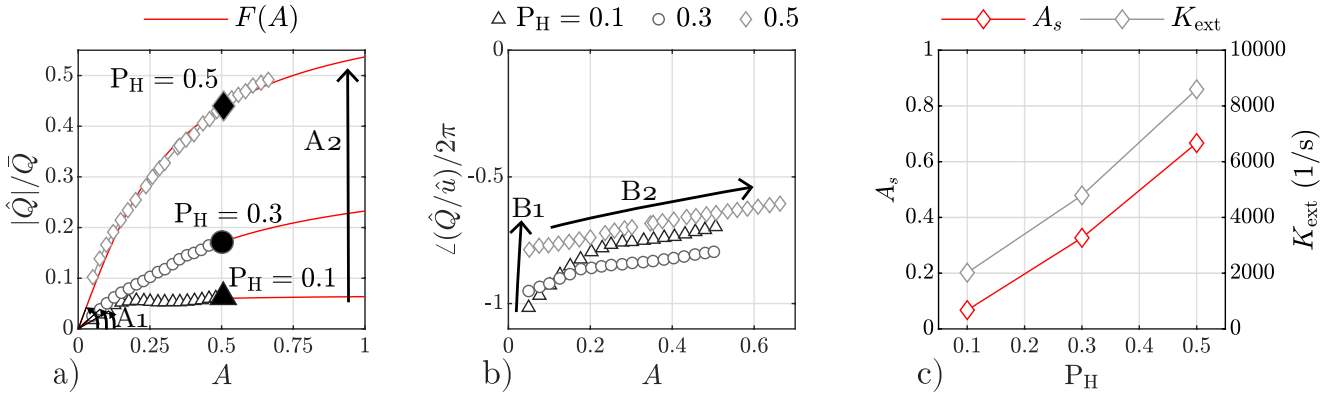

Fig. 6. Relationship between $\hat{Q}$ and A for $f = 1$ kHz. a) Amplitude of the global HRR $|\hat{Q}|/\bar{Q}$. Markers indicate measurements and the lines are represented by Eq. (8). b) Phase difference between $\hat{Q}$ and $\hat{u}$. c) Saturation amplitude A_s and extinction strain rate K_{ext}. The black markers in a) correspond to cases shown in Figs. 9 and 10.

the response changes when P_H is increased. There is an increase in the gain G and the saturation amplitude of $\hat{Q}$ increases. These two trends are annotated by A_1 and A_2 respectively. It should be mentioned that in the measured range, the flame response only shows clear signs of saturation for $P_H = 0.1$ when the response becomes approximately horizontal. Moreover, there is a possibility that the response could increase again for larger values of A if the relationship is non-monotonic. However, at $A = 0.5$, the amplitude of $\hat{Q}$ is increased by an order of magnitude from $P_H = 0.1$ to $P_H = 0.5$. This result indicates that when P_H is increased, an increase in the oscillation amplitude of the flame can be expected, given that the particular frequency is unstable in a system. Previously, we observed this for single [7] and multiple flames [8]. This trend has also been observed in studies on different combustors where hydrogen enrichment leads to an increase in the pressure amplitude and mode frequencies [34; 9; 11; 35; 59].

To extract more information on the saturation amplitude for all cases, the data in Fig. 6 a) is fitted using the model proposed by [60]

$$\hat{Q}/\bar{Q} = F(A) = G_0 \frac{2A}{1+\sqrt{1+(\eta A)^2}}. \tag{8}$$

These fits correspond to the red lines where the gain (slope at $A = 0$) is given by the parameter G_0 and the saturation amplitude is given by the limit

$$A_s = \lim_{A\to\infty} F(A) = 2G_0/\eta. \tag{9}$$

This model assumes a monotonic saturation and cannot describe a non-monotonic response in the gain with increasing A. The saturation amplitudes A_s obtained from the model are shown in Fig. 6 c), which shows an increase with P_H. For $P_H = 0.3$ and 0.5, the saturation amplitude A_s is not reached before $A > 1$ which implies that the velocity amplitude has to exceed the mean flow.

As discussed in the introduction, saturation may be governed by two mechanisms leading to flame surface destruction: vortex roll up and unsteady flame lift up [45; 46]. It will be shown later that the flame anchoring point is fixed across the experiments and hence, the non-linearity is dominated by flame vortex roll up.

One of the mechanisms that can restrict a flame from further growth is that local extinction of the flame surface occurs due to sufficient hydrodynamic flame strain [61]. A flame's capability to withstand flame strain is given by the extinction strain rate K_{ext} which is shown in Fig. 6 c). The

increase in K_{ext} is compared with the increase in A_s and both quantities show similar trends. Hence, a possible explanation for the increase in A_s with P_H is that hydrogen enrichment leads to an increase in K_{ext}. This prevents local extinction of the flame surface and the flame is able to follow the flow fluctuations to larger amplitudes.

Two additional observations can be made by examining the phase difference between $\hat{Q}$ and $\hat{u}$ shown in Fig. 6 b). Firstly, the values of the phase differences at low amplitude are $\angle(\hat{Q}/\hat{u})/2\pi = -1.02, -0.95, -0.79$ for $P_H = 0.1$, 0.3, and 0.5 respectively. This matches reasonably well with the phase estimated from the mean time delay (shown in Table. 1) $-f\tau = -1.23, -1.08, -0.85$, which is based on the mean flame length L_f and velocity $\bar{u}$. As discussed before, an increase in P_H leads to a decrease in the time delay and hence, a decrease in the phase difference, which is annotated by B_1. Secondly, there is a moderate decrease in the phase as A is increased which is annotated by the black arrow labeled by B_2. If the response is governed by vortex roll-up, this decrease in the phase may be caused by the size of the vortex that rolls up along the shear layers which becomes larger for higher forcing amplitudes [62]. In turn, the flame interacts with the flow structure earlier in the phase cycle, i.e., it reduces the time delay and therefore the phase. This is shown to be the case later (see Fig. 11) when the flame images are analysed in detail.

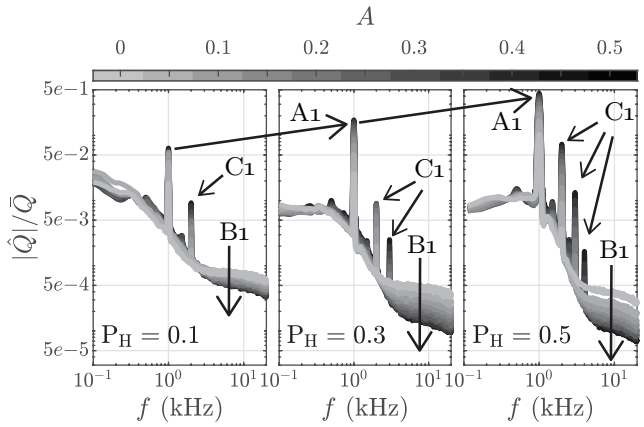

Fig. 7. Energy spectra of the gobal HRR for increasing forcing amplitudes shown at $f = 1$ kHz for $P_H = 0.1, 0.3$ and 0.5.

6 Flame dynamics

In the remaining parts of the paper, the flame dynamics are investigated in detail. The data in Fig. 6 only shows the amplitude and phase taken at the forcing frequency. To investigate the response in more detail, the energy spectra are shown in Fig. 7 for different values of A. The arrows annotated by A_1 show the trend observed in Fig. 6 where an increase in P_H leads to an increase in the amplitude of the peak taken at the forcing frequency. However, two additional observations that can be made are annotated by the letters B_1 and C_1. The arrows annotated by B_1 show that as P_H is increased, there is a decrease in the energy distributed at higher frequencies as A is increased. The arrows annotated by C_1 show that an increase in P_H leads to a significant increase in the energy occurring at higher harmonics of the forcing frequency, i.e. at $2f$, $3f$, $4f$ etc. One possible explanation for these trends is that, as the hydrogen concentration and thus the flame speed and extinction strain rate are increased, the flame becomes more able to respond to the imposed convective structures, i.e. the flame responds quicker to the larger and stronger convective structures imposed by the flow. This in turn, leads to a more coherent response which then manifests as the broad-band energy moving into the forcing frequency and its harmonics.

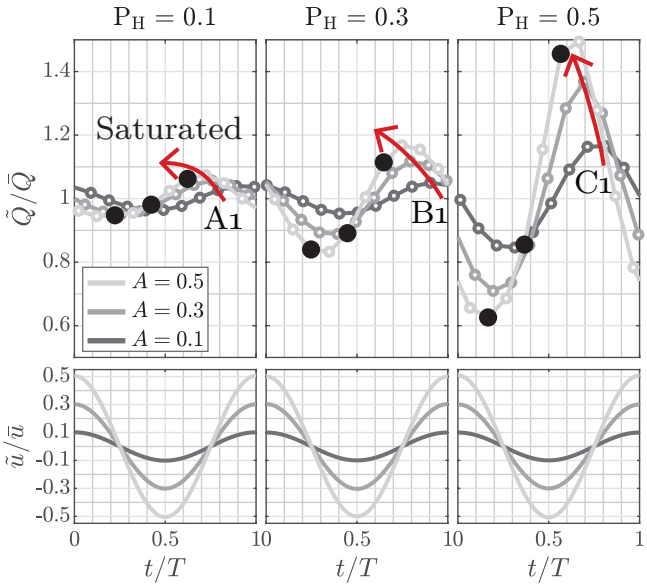

Fig. 8. Time-series of the phase averaged global HRR $\tilde{Q}/\bar{Q}$ and acoustic velocity oscillations $\tilde{u}/\bar{u}$ shown through a full forcing cycle. The black markers correspond to the snapshots viewed in Fig. 9.

6.1 Image analysis

To investigate this change in behaviour in more detail, we analyse the high speed imaging data. First, as a reference, the time-series of the phase averaged global HRR are discussed. These are obtained by integrating the side images and are denoted by a tilde ($\tilde{\cdot}$) and are shown in Fig. 8. The bottom set of panels shows the reconstructed acoustic velocity $\tilde{u}/\bar{u}$ and cases are shown for $A = 0.1$, 0.3, and 0.5. As was shown in Figs. 6 and 7, the amplitude of $\tilde{Q}$ increases with P_H. Also, the phase difference between $\tilde{u}$ and $\tilde{Q}$ decreases with A, as indicated by the red arrows. As mentioned before, this happens because, as the forcing amplitude is increased, the size of the convective structure that is rolled up increases leading to the HRR to occur earlier in the forcing cycle.

For $P_H = 0.1$, the waveform of $\tilde{Q}$ is approximately monochromatic for all values of A and the amplitude has already saturated at $A = 0.3$. For $P_H = 0.3$, the flame has not yet reached saturation at $A = 0.5$, and the waveform steepens which indicates that energy is distributed to higher harmon-

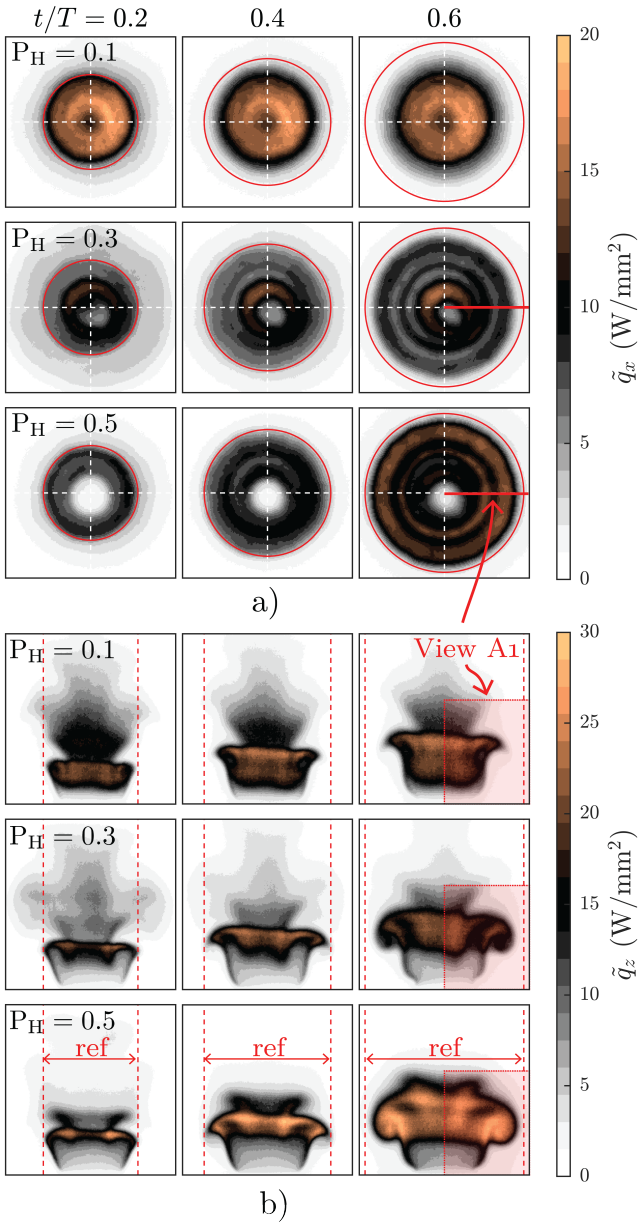

Fig. 9. Image time series of the phase averaged HRR viewed from a) the top $\tilde{q}_x$, and b) the front $\tilde{q}_z$. The time t/T corresponds to the black dots in Fig. 8 for $A = 0.5$. The red circles and lines indicate the expansion of the flame for $P_H = 0.5$. View A_1 corresponds to the region shown in Fig. 10.

ics of f. This process intensifies for $P_H = 0.5$, where the waveform of $\tilde{Q}$ steepens significantly. At $t/T = 0.6$, the increase in the HRR occurs more in a burst compared to lower values of P_H.

More information is revealed when viewing the flame structure from the top and side simultaneously. Fig. 9 a) and b) show the phase averaged flame $\tilde{q}_x$ (top) and $\tilde{q}_z$ (side) at three phase instances $t/T = 0.2$, 0.4, and 0.6. These instances correspond to parts of the cycle where the HRR transitions from a minimum to a maximum and correspond to the black symbols in Fig. 8 taken at $A = 0.5$. The phase $t/T = 0$ corresponds to the phase where the maximum acoustic velocity occurs, i.e. $\max_t(\tilde{u})$

Significant differences in the HRR distributions are observed by examining the images taken from the top. At $P_H = 0.1$, a large portion of the total HRR is distributed throughout the volume above the recirculation zone (this is more clearly shown in the PLIF data in Figs. 10 and 11). Furthermore, the HRR does not vary significantly between the frames. This indicates that a large portion of the HRR remains incoherent with the forcing frequency consistent with a large turbulent flame brush. As P_H is increased, the spatial distribution of the HRR changes significantly. At $P_H = 0.3$ and 0.5, the HRR becomes more radially compact with little to no HRR occurring in the centre of the combustor. There are larger variations between the frames and the radius of the flame front position increases significantly with t/T. As a reference the radius for the case at $P_H = 0.5$ is indicated by a red circle and as P_H is increased, this radius increases.

To understand why this occurs, the side images in Fig. 9 b) are now examined. The position of the red circle is indicated by the red dotted vertical lines annotated ref. Again, for $P_H = 0.1$, most of the HRR is distributed at the centre of the flame and there is not a significant growth outwards throughout the forcing cycle. As P_H is increased, the growth of the radius increases and along with this growth, large vortex structures are formed along the outer shear layer of the jet. This leads to a burst of HRR at $t/T = 0.6$ that occurs around the whole circumference of the flame. From the top, these bursts appear as concentric rings of high intensity.

6.2 Kinematic of flame vortex roll-up

The side images show clear signs of flame vortex roll up, but only provide a line of sight view of the process. To get a more detailed view, OH-PLIF images were obtained for the same conditions in the $x-y$ plane. These were then used to compute the phase averaged flame surface density (FSD) and the corresponding phase averaged curvature distributions. The views correspond to the red areas annotated View A_1 in Fig. 9 and are shown in Fig. 10. The curvature is only shown for FSD > 1W/mm^3. As a reference, the convective velocity wave is indicated by the red lines. The locations of minimum and maximum velocity are indicated by the horizontal dotted lines annotated in the upper left panel.

For all cases, as t/T progresses, the maximum of the velocity wave starts at the dump plane and then convects downstream at velocity $\bar{u}$. As the velocity wave propagates, first a large structure rolls the flame in towards the inner recirculation zone. This process is annotated by a black arrow and the letter A_1. For $P_H = 0.1$ (frames in rows 1 and 4), the flame is completely rolled in over itself and the flame is quenched in the inner recirculation zone. This process causes the flame to burn as a turbulent flame brush inside the recirculation zone which significantly reduces the flame's ability to respond to the large amplitude forcing and explains the small variation between frames in Fig. 9. As P_H is increased, this process changes significantly. For $P_H = 0.3$ (frames in rows 2 and 5), the size of the flame structure that rolls up towards the inner zone is reduced and the size of the turbulent flame brush

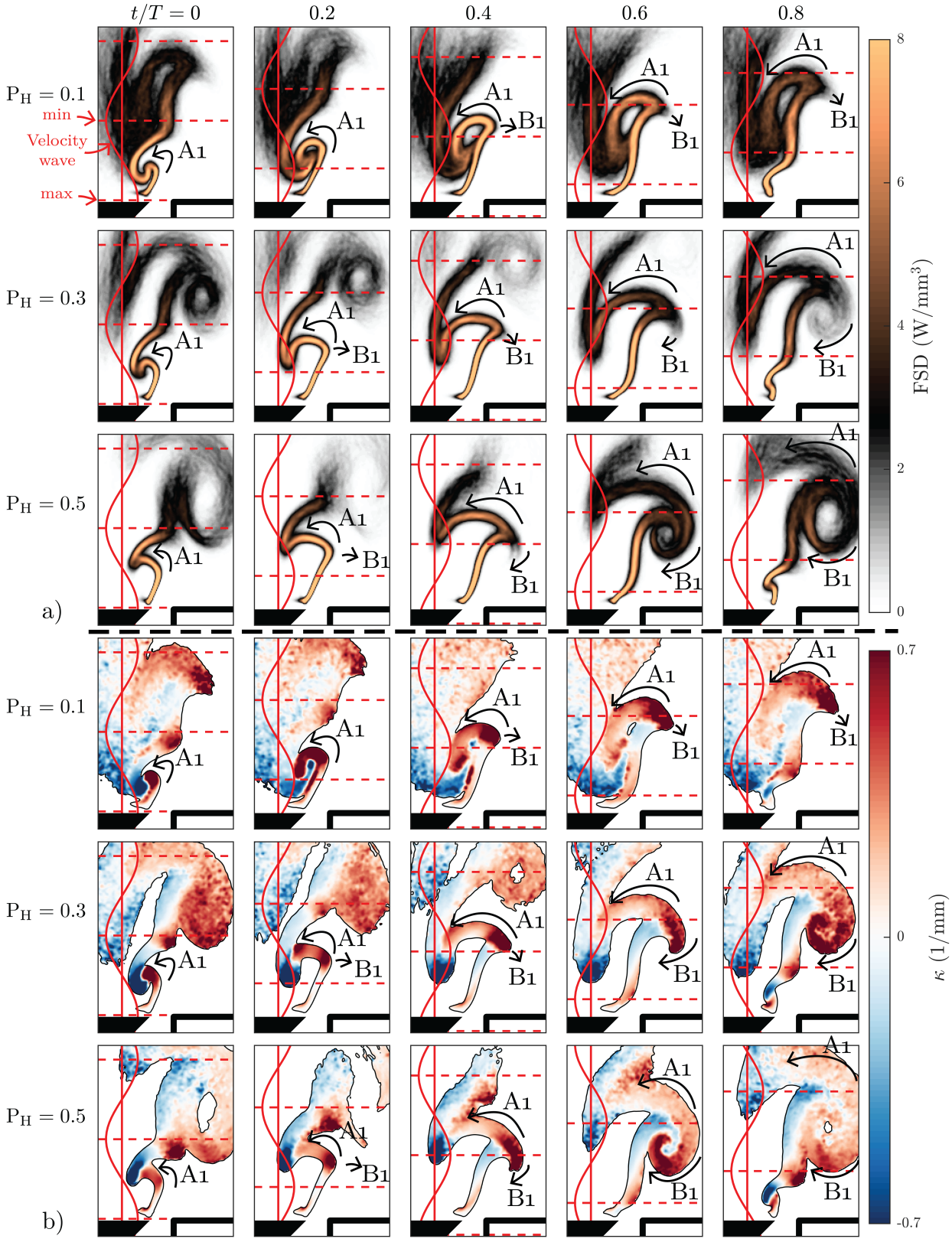

Fig. 10. Phase averaged flame surface density (FSD) coloured by the flame curvature κ, shown through the forcing cycle for $A = 0.5$. Annotation A_1) shows the flame roll-up process towards the inner shear layer. Annotation B_1) shows the flame roll-up process towards the outer shear layer.

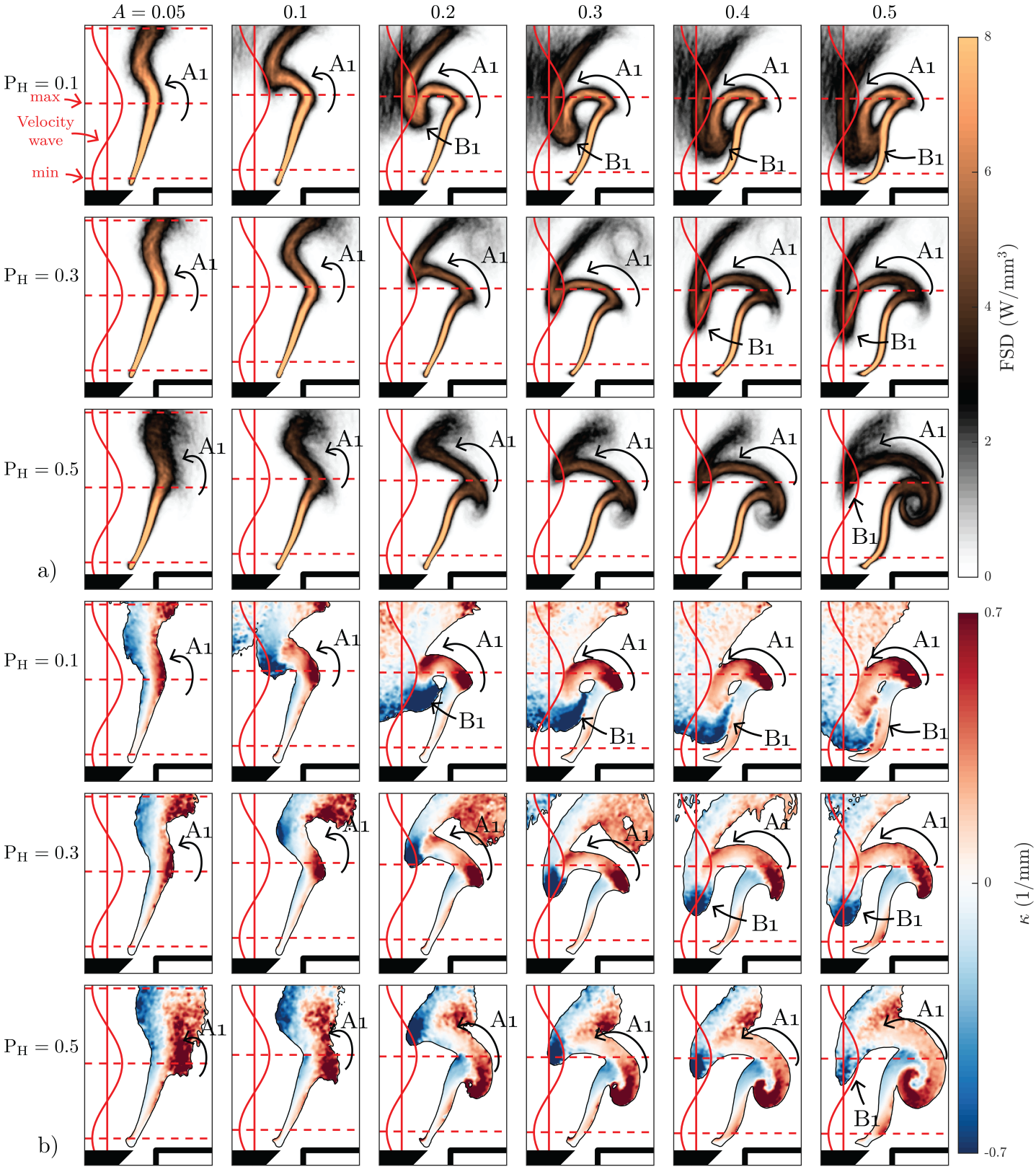

Fig. 11. Phase averaged flame surface density (FSD) coloured by the flame curvature κ, shown at different amplitudes A at $t/T = 0.6$.

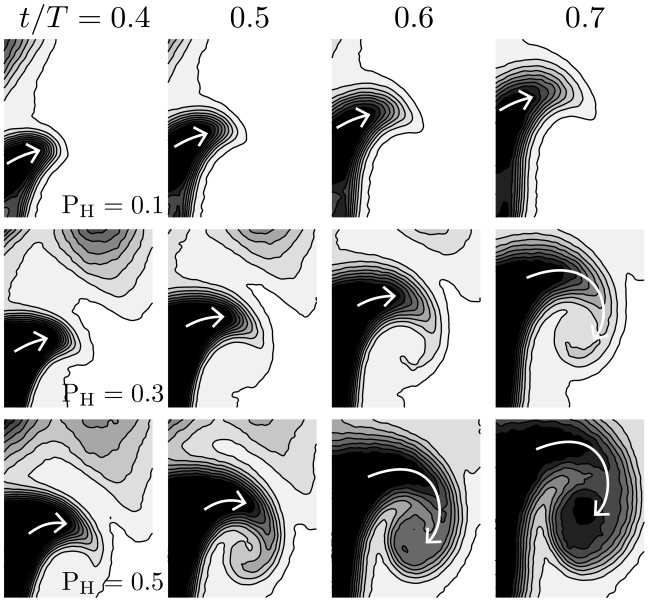

Fig. 12. Phase averaged OH-PLIF images at $A = 0.5$ for $t/T = 0.4$, 0.5, 0.6, 0.7, indicating the movement of the flames leading edge towards the outer recirculation zone.

is decreased. This trend continues for $P_H = 0.5$ (frames in rows 3 and 6), and may be caused by the significant increase in the extinction strain rate as was shown in Fig. 6 c).

At $t/T > 0.2$ (second column) there is a second process that starts to emerge. This process is annotated by the letter B_1 and indicates the movement of the flame tip out towards the outer part of the jet. For $P_H = 0.1$, the flame is not able to progress significantly, whereas for $P_H = 0.3$ and 0.5, the flame is able to propagate across the jet. Then, after crossing the jet, the flame consumes the unburned reactants in the vortex structure rolling up the outer shear layer. This process explains the movement of the HRR radially outwards as seen from above in Fig. 9. At $P_H = 0.5$ this process happens significantly quicker compared to $P_H = 0.3$, and the flame is able to consume all the fuel in the outer vortex in a burst shown at $t/T = 0.6$ (fourth column). This behaviour explains the two observations in Fig. 7 where 1) (annotated B_1) an increase in P_H leads to a decrease in the energy distributed at higher frequencies and 2) (annotated C_1) more energy gets distributed into the harmonics of the forcing frequency. At $P_H = 0.1$, the flame quenches in the inner recirculation zone and burns as a turbulent flame brush and hence, the distribution of energy at higher frequencies is still incoherent and evenly distributed across the frequencies. As P_H is increased and the flame consumes the outer vortex structure in a burst, this leads to the steepening of the signals in Fig. 8, which indicates that the energy that was distributed at higher frequencies becomes coherent with the forcing frequency and its harmonics. As P_H is increased further to $P_H = 0.5$, the increase in flame speed causes this process to occur faster and hence, more of the energy can become coherent with the forcing frequency.

It has been shown that hydrogen enriched flames at lean conditions feature flame speed that significantly varies with the strain rate [1; 5]. Due to differential diffusion, the leading edges tend to accelerate towards the unburned reactants. Although most of these studies focus on small scales, the dynamics observed in this study suggest that the large scale structures also feature very similar dynamics. In Fig. 10 b) (rows 4-6) the curvature distribution shows how the flame vortex interaction significantly wrinkles the flame, resulting in leading edges with large positive and negative curvature. The high level of curvature indicates large strain rates along the flame front. It is observed that as P_H is increased, the flame becomes significantly more resilient against being pulled into the inner recirculation zone and quench due to the increased extinction strain rate.

At $t/T = 0.4$ (third column), the leading edge annotated by B_1 moves towards the outer shear layer of the jet. As P_H is increased , this movement accelerates and could be explained by the increased flame speed due to the differential diffusion of hydrogen. To highlight this effect, phase averaged OH-PLIF images are shown in a region zoomed in on the flame's leading edge in Fig. 12. For an increasing level of P_H, the flame tip accelerates across the jet and is able to consume the outer vortex in a burst. Subsequently, this leads to a significant increase in the HRR fluctuations and hence, a large amplitude response in the FDF.

The images in Figs. 10 and 12 are only shown at $A = 0.5$, i.e. at a high forcing amplitude. To view the progressive effect of increasing the forcing amplitude, snapshots of the flame front are shown at $t/T = 0.6$ in Fig. 10. Moving from left to right the forcing amplitude is increased from $A = 0.05$ to 0.5. As such, the figure shows how the flame front gets progressively more contorted by the convective structure formed by the acoustic forcing.

At low forcing amplitude $A = 0.05$ the three cases show a reasonably similar flame structure. As A is increased, the flame starts to get pulled into the recirculating zone due to the interaction with the vortex structure that rolls up along the inner shear layer. As before, this contortion is annotated by the arrow A_1. Comparing the three blends at the same value of A shows that the flame becomes significantly more contorted at lower hydrogen concentrations. Moreover, for $P_H = 0.1$, the image of the flame is more or less unchanged for $A > 0.1$, which indicates that the response has saturated. This is consistent with the fluctuation of global HRR shown previously in Fig. 6a). As mentioned before, this is caused by the flame front reaching the extinction strain rate which limits the flame response. The location where this occurs is annotated by B_1. For $P_H = 0.3$, the flame structure starts to look similar for $A > 0.4$, indicating that saturation will occur at higher A. For $P_H = 0.5$, the flame structure continues to develop over the full range of A.

The second process that also changes with P_H is the growth of HRR in the outer resirculation zone where the outer vortex is formed. For $P_H = 0.1$ the flame front is not able to propagate across the jet for any values of A. As P_H is increased, this development changes progressively where for $P_H = 0.3$, the flame propagates across the shear layer for $A > 0.3$. At $P_H = 0.5$, this progression occurs quicker and the flame propagates across the shear layer already at $A > 0.1$.

Moreover, the size of the vortex structure that is consumed, continues to increase over the full range of A without a clear indication of the onset of saturation before $A = 1$ according to the model. This is potentially significant as it suggests that saturation may only occur when the amplitude of the velocity fluctuations approaches or exceeds the mean velocity in flames with high hydrogen concentrations (with the caveat that this result is for a specific set of operating conditions and a fixed forcing frequency).

7 Conclusions

In this paper we investigate the effect of hydrogen enrichment on the flame response submitted to large amplitude acoustic excitation. At constant nozzle bulk velocity and thermal power, thereby at similar hydrodynamics, the behavior of the flame for increasing hydrogen enrichment was investigated. Three methane/hydrogen blends ranging from $10 - 50\%$ hydrogen by power were investigated and the flame describing function (FDF) was measured for a single frequency. Measurements of the global heat release rate show that hydrogen enrichment leads to a significant increase in the amplitude level of the heat release rate oscillations. An increase in the hydrogen concentration also leads to a decrease in the energy distributed at larger frequencies and a corresponding growth of energy at higher harmonics of the forcing frequency, as the amplitude of forcing was increased.

These observations were investigated through high-speed imaging combined with OH-PLIF to obtain a detailed view of the convective roll-up process of the flame front. At large amplitudes, this interaction leads to non-linear saturation of the global heat release rate. The analysis shows that at lower hydrogen concentration, the flame front rolls up along the inner shear layer and is quenched in the inner recirculation zone. This process leads to remaining fuel that burns as a turbulent incoherent brush, reducing the amplitude of the global flame response at higher acoustic forcing amplitudes. When increasing the hydrogen concentration, the flame is more resilient against this process, which may be caused by an increase in the extinction strain rate. Moreover, when increasing the hydrogen concentration, the flame tip accelerates and is able to propagate across the two shear layers of the jet and consume fuel accumulated in the outer vortex structure. This change in dynamics may be caused by the significant increase in the flame speed and the additional acceleration of the flame leading edge due to the differential diffusion of hydrogen. The process significantly increases the coherent consumption of unburnt mixture and hence, substantially increases the oscillation amplitude of the flame and consequently pressure.

It is well known that increasing the hydrogen content in the fuel of premixed flames leads to challenges with respect to NO_x-emissions and flashback, and recent studies also suggest they can increase the likelihood of thermoacoustic oscillations. This paper shows that increasing hydrogen content increases the amplitude of the velocity fluctuations at which the flame saturates. Although our experiments were conducted on a simple bluff body geometry, it is reasonable to expect that similar trends will be observed in swirling premixed flames noting that differences in the flame response and saturation behaviour will be modified by the addition of an azimuthal velocity component which changes the flame shape and characteristic velocity and time-scales.

Acknowledgments

The authors acknowledge support from the NCCS Centre, funded under the Norwegian research program, Centres for Environment-friendly Energy Research (FME) (Grant 257579/E20) and the European Union's Horizon 2020 research and innovation program ANNULIGhT (Grant 765998).

References

[1] Hochgreb, S., 2022. "How fast can we burn, 2.0". *Proc Combust Inst*.

[2] Korol, G., Kumar, R., and Bowles, E., 1993. "Burning velocities of hydrogen-air mixtures". *Combust Flame,* **94**(3), Aug., pp. 330–340.

[3] Boushaki, T., Dhué, Y., Selle, L., Ferret, B., and Poinsot, T., 2012. "Effects of hydrogen and steam addition on laminar burning velocity of methane–air premixed flame: Experimental and numerical analysis". *Int. J. Hydrog. Energy,* **37**(11), June, pp. 9412–9422.

[4] Beerer, D., Mcdonell, V., P., T., and K., C. R., 2013. "Flashback and turbulent flame speed measurements in hydrogen/methane flames stabilized by a low-swirl injector at elevated pressures and temperatures". *J. Eng. Gas Turbines Power,* **136**(3), Nov.

[5] Rieth, M., Gruber, A., Williams, F. A., and Chen, J. H., 2022. "Enhanced burning rates in hydrogen-enriched turbulent premixed flames by diffusion of molecular and atomic hydrogen". *Combust Flame,* **239**, p. 111740.

[6] Berger, L., Attili, A., and Pitsch, H., 2022. "Synergistic interactions of thermodiffusive instabilities and turbulence in lean hydrogen flames". *Combust Flame,* **244**, p. 112254.

[7] Aguilar, J. G., Æsøy, E., and Dawson, J. R., 2022. "The influence of hydrogen on the stability of a perfectly premixed combustor". *Combust Flame,* **245**, p. 112323.

[8] Æsøy, E., Indlekofer, T., Gant, F., Cuquel, A., Bothien, M. R., and Dawson, J. R., 2022. "The effect of hydrogen enrichment, flame-flame interaction, confinement, and asymmetry on the acoustic response of a model can combustor". *Combust Flame,* **242**, p. 112176.

[9] Lee, T., and Kim, K. T., 2020. "Combustion dynamics of lean fully-premixed hydrogen-air flames in a mesoscale multinozzle array". *Combust Flame,* **218**, Aug., pp. 234–246.

[10] Kang, H., and Kim, K. T., 2021. "Combustion dynamics of multi-element lean-premixed hydrogen-air flame ensemble". *Combust Flame,* **233**, Nov., p. 111585.

[11] Lee, T., and Kim, K. T., 2022. "High-frequency transverse combustion instabilities of lean-premixed multi-

slit hydrogen-air flames". *Combust Flame,* **238**, Apr., p. 111899.

[12] Yahou, T., Dawson, J. R., and Schuller, T., 2022. "Impact of chamber back pressure on the ignition dynamics of hydrogen enriched premixed flames". *Proc Combust Inst*.

[13] Aniello, A., Poinsot, T., Selle, L., and Schuller, T., 2022. "Hydrogen substitution of natural-gas in premixed burners and implications for blow-off and flashback limits". *Int. J. Hydrog. Energy,* **47**(77), pp. 33067–33081.

[14] Chiesa, P., Lozza, G., and Mazzocchi, L., 2005. "Using hydrogen as gas turbine fuel". *J. Eng. Gas Turbines Power,* **127**(1), Jan., pp. 73–80.

[15] Bothien, M. R., Ciani, A., Wood, J. P., and Fruechtel, G., 2019. "Toward decarbonized power generation with gas turbines by using sequential combustion for burning hydrogen". *J. Eng. Gas Turbines Power,* **141**(12), Nov.

[16] European Turbine Network, 2020. Hydrogen and gas turbines: The path towards a zero-carbon gas turbine. Tech. rep., ETN Global.

[17] Beita, J., Talibi, M., Sadasivuni, S., and Balachandran, R., 2021. "Thermoacoustic instability considerations for high hydrogen combustion in lean premixed gas turbine combustors: A review". *Hydrogen,* **2**(1), Jan., pp. 33–57.

[18] Bothien, M. R., Noiray, N., and Schuermans, B., 2014. "A novel damping device for broadband attenuation of low-frequency combustion pulsations in gas turbines". *J. Eng. Gas Turbines Power,* **136**(4).

[19] Kim, K. T., Lee, J., Lee, H. J., Quay, B. D., and Santavicca, D. A., 2010. "Characterization of forced flame response of swirl-stabilized turbulent lean-premixed flames in a gas turbine combustor". *J. Eng. Gas Turbines Power,* **132**(4), Jan.

[20] Davis, D., Therkelsen, P., Littlejohn, D., and Cheng, R., 2013. "Effects of hydrogen on the thermo-acoustics coupling mechanisms of low-swirl injector flames in a model gas turbine combustor". *Proc Combust Inst,* **34**(2), Jan., pp. 3135–3143.

[21] Shanbhogue, S. J., Sanusi, Y., Taamallah, S., Habib, M., Mokheimer, E., and Ghoniem, A. F., 2016. "Flame macrostructures, combustion instability and extinction strain scaling in swirl-stabilized premixed CH4/H2 combustion". *Combust Flame,* **163**, Jan., pp. 494–507.

[22] Chterev, I., and Boxx, I., 2021. "Effect of hydrogen enrichment on the dynamics of a lean technically premixed elevated pressure flame". *Combust Flame,* **225**, Mar., pp. 149–159.

[23] Mao, R., Wang, J., Lin, W., Han, W., Zhang, W., and Huang, Z., 2022. "Effects of flow-flame interactions on the stabilization of ultra-lean swirling ch_4/h_2/air flames". *Fuel,* **319**, July, p. 123619.

[24] Guiberti, T. F., Durox, D., Scouflaire, P., and Schuller, T., 2015. "Impact of heat loss and hydrogen enrichment on the shape of confined swirling flames". *Proc Combust Inst,* **35**(2), pp. 1385–1392.

[25] Schuller, T., Poinsot, T., and Candel, S., 2020. "Dynamics and control of premixed combustion systems based on flame transfer and describing functions". *J. Fluid Mech.,* **894**.

[26] Æsøy, E., Aguilar, J. G., Wiseman, S., Bothien, M. R., Worth, N. A., and Dawson, J. R., 2020. "Scaling and prediction of transfer functions in lean premixed h2/ch4-flames". *Combust Flame,* **215**, pp. 269–282.

[27] Æsøy, E., Aguilar, J. G., Bothien, M. R., Worth, N. A., and Dawson, J. A., 2021. "Acoustic-convective interference in transfer functions of methane/hydrogen and pure hydrogen flames". *J. Eng. Gas Turbines Power*, July.

[28] Ghani, A., and Polifke, W., 2021. "Control of intrinsic thermoacoustic instabilities using hydrogen fuel". *Proc Combust Inst,* **38**(4), pp. 6077–6084.

[29] Casel, M., and Ghani, A., 2022. "Analysis of the flame dynamics in methane/hydrogen fuel blends at elevated pressures". *Proc Combust Inst*.

[30] Lim, Z., Li, J., and Morgans, A. S., 2021. "The effect of hydrogen enrichment on the forced response of ch4/h2/air laminar flames". *Int. J. Hydrog. Energy,* **46**(46), pp. 23943–23953.

[31] Æsøy, E., Nygård, H. T., Worth, N. A., and Dawson, J. R., 2022. "Tailoring the gain and phase of the flame transfer function through targeted convective-acoustic interference". *Combust Flame,* **236**, p. 111813.

[32] Æsøy, E., Jankee, G. K., Yadala, S., Worth, N. A., and Dawson, J. R., 2022. "Suppression of self-excited thermoacoustic instabilities by convective-acoustic interference". *Proc Combust Inst*.

[33] Park, D., Lee, T., and Kim, K. T., 2022. "Rotational symmetry-driven modal dynamics of high-frequency transverse instabilities in a lean-premixed multislit hydrogen combustor". *Combust Flame,* **245**, p. 112356.

[34] Kang, H., Lee, M., and Kim, K. T., 2022. "Measurements of self-excited instabilities and nitrogen oxides emissions in a multi-element lean-premixed hydrogen/methane/air flame ensemble". *Proc Combust Inst*.

[35] Indlekofer, T., Ahn, B., Kwah, Y. H., Wiseman, S., Mazur, M., Dawson, J. R., and Worth, N. A., 2021. "The effect of hydrogen addition on the amplitude and harmonic response of azimuthal instabilities in a pressurized annular combustor". *Combust Flame,* **228**, pp. 375–387.

[36] Indlekofer, T., Faure-Beaulieu, A., Noiray, N., and Dawson, J. R., 2021. "The effect of dynamic operating conditions on the thermoacoustic response of hydrogen rich flames in an annular combustor". *Combust Flame,* **223**, pp. 284–294.

[37] Æsøy, E., Indlekofer, T., Gant, F., Cuquel, A., Bothien, M. R., and Dawson, J., 2022. "The effect of hydrogen enrichment, flame-flame interaction, confinement, and asymmetry on the acoustic response of a model can combustor". *Combust Flame,* **242**, p. 112176.

[38] Oztarlik, G., Selle, L., Poinsot, T., and Schuller, T., 2020. "Suppression of instabilities of swirled premixed flames with minimal secondary hydrogen injection".

Combust Flame, **214**, Apr., pp. 266–276.

[39] Schuller, T., Marragou, S., Oztarlik, G., Poinsot, T., and Selle, L., 2022. "Influence of hydrogen content and injection scheme on the describing function of swirled flames". *Combust Flame,* **240**, p. 111974.

[40] Laera, D., Agostinelli, P. W., Selle, L., Cazères, Q., Oztarlik, G., Schuller, T., Gicquel, L., and Poinsot, T., 2021. "Stabilization mechanisms of CH4 premixed swirled flame enriched with a non-premixed hydrogen injection". *Proc Combust Inst,* **38**(4), pp. 6355–6363.

[41] Noiray, N., Durox, D., Schuller, T., and Candel, S., j. v. p. y. p. "A unified framework for nonlinear combustion instability analysis based on the flame describing function".

[42] Durox, D., Schuller, T., Noiray, N., and Candel, S., 2009. "Experimental analysis of nonlinear flame transfer functions for different flame geometries". *Proc Combust Inst,* **32**(1), pp. 1391–1398.

[43] O'Connor, J., 2022. "Understanding the role of flow dynamics in thermoacoustic combustion instability". *Proc Combust Inst*.

[44] Schadow, K. C., and Gutmark, E. "Combustion instability related to vortex shedding in dump combustors and their passive control". *PECS*.

[45] Balachandran, R., Ayoola, B., Kaminski, C., Dowling, A., and Mastorakos, E., 2005. "Experimental investigation of the nonlinear response of turbulent premixed flames to imposed inlet velocity oscillations". *Combust Flame,* **143**(1-2), pp. 37–55.

[46] Bellows, B. D., Bobba, M. K., Forte, A., Seitzman, J. M., and Lieuwen, T., 2007. "Flame transfer function saturation mechanisms in a swirl-stabilized combustor". *Proc Combust Inst,* **31**(2), pp. 3181–3188.

[47] Bellows, B. D., Bobba, M. K., Seitzman, J. M., and Lieuwen, T., 2006. "Nonlinear Flame Transfer Function Characteristics in a Swirl-Stabilized Combustor". *J. Eng. Gas Turbines Power,* **129**(4), 12, pp. 954–961.

[48] Æsøy, E., 2022. "The effect of hydrogen enrichment on the thermoacoustic behaviour of lean premixed flames". PhD thesis.

[49] Seybert, A. F., and Ross, D. F., 1977. "Experimental determination of acoustic properties using a two-microphone random-excitation technique". *J. Acoust.,* **61**(5), May, pp. 1362–1370.

[50] Higgins, B., McQuay, M. Q., Lacas, F., Rolon, J.-C., Darabiha, N., and Candel, S., 2001. "Systematic measurements of oh chemiluminescence for fuel-lean, high-pressure, premixed, laminar flames". *Fuel,* **80**(1), pp. 67–74.

[51] Wiseman, S., Gruber, A., and Dawson, J. R., 2022. "Flame transfer functions for turbulent, premixed, ammonia-hydrogen-nitrogen-air flames submitted for publication". *J. Eng. Gas Turbines Power*.

[52] Worth, N. A., and Dawson, J. R., 2012. "Cinematographic oh-plif measurements of two interacting turbulent premixed flames with and without acoustic forcing". *Combust Flame,* **159**(3), pp. 1109–1126.

[53] Goodwin, D. G., Moffat, H. K., and Speth, R. L., 2015. "Cantera: An object-oriented software toolkit for chemical kinetics, thermodynamics, and transport processes. version 2.2.0". *Zenodo*.

[54] Kutkan, H., Amato, A., Campa, G., Ghirardo, G., Tay Wo Chong, L., and Æsøy, E., 2022. "Modeling of turbulent premixed ch4/h2/air flames including the influence of stretch and heat losses". *J. Eng. Gas Turbines Power,* **144**(1).

[55] Garcia, A. M., Bras, S. L., and Polifke, W., 2022. "Effect of hydrogen addition on the consumption speed of lean premixed laminar methane flames exposed to combined strain and heat loss". *arXiv preprint arXiv:2211.15171*.

[56] Wiseman, S., Rieth, M., Gruber, A., Dawson, J. R., and Chen, J. H., 2021. "A comparison of the blow-out behavior of turbulent premixed ammonia/hydrogen/nitrogen-air and methane–air flames". *Proc Combust Inst,* **38**(2), pp. 2869–2876.

[57] Poinsot, T., and Veynante, D., 2005. *Theoretical and numerical combustion*. RT Edwards, Inc.

[58] Balachandran, R., Ayoola, B., C., K., A., D., and E., M., 2005. "Experimental investigation of the nonlinear response of turbulent premixed flames to imposed inlet velocity oscillations". *Combust Flame,* **143**(1-2), Oct., pp. 37–55.

[59] Zhang, J., and Ratner, A., 2021. "Experimental study of the effects of hydrogen addition on the thermoacoustic instability in a variable-length combustor". *Int. J. Hydrog. Energy,* **46**(29), Apr., pp. 16086–16100.

[60] Ghirardo, G., Gant, F., Boudy, F., and Bothien, M. R., 2021. "Protection and identification of thermoacoustic azimuthal modes". *J. Eng. Gas Turbines Power,* **143**(4).

[61] Lieuwen, T., 2021. *Unsteady combustor physics*. CUPS.

[62] Aydemir, E., Worth, N. A., and Dawson, J. R., 2012. "The formation of vortex rings in a strongly forced round jet". *Exp Fluids,* **52**, pp. 729–742.